Influence of spin orbit splitting and satellite transitions on nickel soft X-ray optical properties near its $L_{2,3}$ absorption edge region

Kiranjot,[a,b] Mohammed H. Modi,[a,b]* Raj Kumar Gupta,[b] Mangalika Sinha[b,c] and Praveen Kumar Yadav[a,b]

[a]Homi Bhabha National Institute, Training School Complex, Anushakti Nagar, Mumbai, Maharashtra 400094, India, [b]Soft X-ray Applications Laboratory, Raja Ramanna Centre for Advanced Technology, Indore, Madhya Pradesh 452013, India, and [c]DESY, Notkestrasse 85, Hamburg 22067, Germany. *Correspondence e-mail: modimh@rrcat.gov.in

Transition elements exhibit strong correlations and configuration interactions between core and valence excited states, which give rise to different excitations inside materials. Nickel exhibits satellite features in its emission and absorption spectra. Effects of such transitions on the optical constants of nickel have not been reported earlier and the available database of Henke et al. does not represent such fine features. In this study, the optical behaviour of ion beam sputter deposited Ni thin film near the $L_{2,3}$-edge region is investigated using reflection spectroscopy techniques, and distinct signatures of various transitions are observed. The soft X-ray reflectivity measurements in the 500–1500 eV photon energy region are performed using the soft X-ray reflectivity beamline at the Indus-2 synchrotron radiation source. Kramers–Kronig analysis of the measured reflectivity data exhibit features corresponding to spin orbital splitting and satellite transitions in the real and imaginary part of the refractive index (refraction and absorption spectra). Details of fine features observed in the optical spectra are discussed. To the best of our knowledge, this is the first study reporting fine features in the measured optical spectra of Ni near its $L_{2,3}$-edge region.

1. Introduction

Precise knowledge of the optical properties of a material is essential in order to make proper and effective use in actual devices. Such knowledge helps in finding suitable applications of materials in various optical components. In the X-ray region, information on optical properties is not readily available for most materials. A comprehensive tabulation of optical constants was generated by Henke et al. (Henke et al., 1993) where optical constants for materials with $Z = 1$ to 92 in the energy range 10–30000 eV are compiled. Moreover, their data mostly rely on absorption measurements and theoretical calculations; thereby it has been found many times that the tabulated data vary especially near absorption edges (Filatova et al., 1996, 1999). These data are reliable in the region away from the absorption thresholds. Near the absorption edges, the refractive index is sensitive to the chemical environment, so any change in the local environment of an atom will also affect the optical parameters. The poor reliability of available data and the lack of experimentally measured data for most materials have attracted researchers to generate more reliable optical datasets, particularly in the case of EUV/soft X-rays, where the K-edges of low-Z elements and the L- and M-edges of high-Z materials occur and give rise to many fine features.
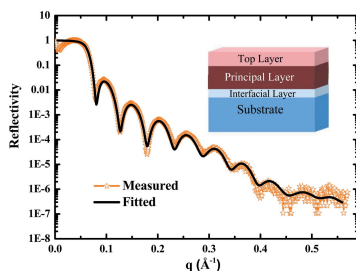
Therefore, the experimental determination of optical properties of potential materials becomes necessary.

Nickel is a transition element used mainly for making different alloys and corrosion-resistant coatings. In the X-ray region, the high reflectivity of Ni makes it useful for making optical components for synchrotron radiation and FEL-based beamlines. It has been used for edge filters in conventional X-ray sources and also as coating materials for suppressing higher-order harmonics in synchrotron beamlines (Waki *et al.*, 1989; Modi *et al.*, 2019). Nickel finds applications in hard X-ray telescopes (Spiga *et al.*, 2004) and normal-incidence optics (Spiga *et al.*, 2004; Takenaka *et al.*, 1996; Sella *et al.*, 1988; Peng *et al.*, 2016). It has also been used as a cladding layer in hard X-ray waveguides (Lagomarsino *et al.*, 1996). The design and actual performances of such types of devices may vary significantly especially near the edge region due to lack of knowledge of optical behaviour. Near the edge region, one can make efficient devices provided information about the optical constants is known precisely (Cruz *et al.*, 2004). In the case of nickel, the existence of charge transfer and multiplet effects near the $2p$ and $3p$ core level regions is observed in absorption measurements (Jo & Sawatzky, 1991; Chen *et al.*, 1991; Tjeng *et al.*, 1993; Magnuson *et al.*, 1998; Ufuktepe *et al.*, 2011). Such multiplet effects in the core level transitions are simply being ignored in its soft X-ray optical properties near the $L_{2,3}$-edge region. It can be realized that nickel optical spectra near the $2p$ region may bear signature of multiplet effects in core level transitions and also effects of strong interaction between valence and core holes. Consideration of such effects will give additional features at energies above the absorption edge and therefore the optical constants must reflect all these fine features. In the available database of Henke *et al.* such fine features are not present. Few studies are available in the literature on optical constants of Ni in the VUV/soft X-ray region. Diel *et al.* have measured optical constants of nickel film in the 40–700 eV energy region (Diel *et al.*, 1997). Xu *et al.* have measured the reflection electron energy loss spectra (REELS) and derived optical constants up to 200 eV of magnetron sputtered nickel thin film (Xu *et al.*, 2017). The validity of results was verified using a theoretical model based on the reverse Monte Carlo (RMC) simulation of electron transport in a solid. In the literature, the behaviour of nickel optical properties near the $L_{2,3}$-edge (850–875 eV) region has not been explored.

Optical constants of a material can be obtained by transmission, reflection and electron energy loss spectroscopy *etc.* In transmission spectroscopy, the absorption of the sample is measured and dispersion is calculated from Kramers–Kronig relations (Delmotte *et al.*, 2018). In reflection spectroscopy, the optical constants can be found by fitting of angle-dependent reflectivity data (Singh *et al.*, 2018), as well as by carrying out Kramers–Kronig analysis of the energy-dependent reflectivity data (Sinha *et al.*, 2018). In the present study, we have used reflection spectroscopy techniques to obtain optical constants of an ion beam sputtered Ni film in the energy range 500–1500 eV. To the best of our knowledge, ours is the first experimental investigation of the optical constants of nickel

near the $L_{2,3}$-edge regions. The fine features in the obtained optical constants profile are explained from known electronic transitions in nickel.

2. Experimental procedure

2.1. Sample preparation

A 100 Å-thick Ni film was deposited on a silicon substrate using the ion beam sputtering system. Prior to deposition, the substrate was ultrasonically cleaned. A commercially available 4-inch diameter Ni target of 99.99% purity was used for deposition and argon gas of 99.99999% purity was used as a sputtering media. Before the deposition process, a base pressure in the chamber of 1.9×10^{-6} mbar was obtained. With Ar at 3 sccm (standard cubic centimetre per minute) flow rate, a pressure of 6.3×10^{-4} mbar was maintained in the chamber. Film thickness and deposition rate were monitored using a quartz crystal thickness monitor.

2.2. Characterizations

Structural characterization of the sample was carried out using a grazing-incidence X-ray reflectivity (GIXRR) technique. A Bruker D-8 system with Cu $K\alpha$ source was used in θ–2θ geometry. The obtained spectrum was fitted using the Parratt recursive formalism (Parratt, 1954). The roughness effect was taken into account using the Névot Croce model (Croce & Névot, 1976).

Compositional analysis of the Ni thin film was carried out using the X-ray photoelectron spectroscopy (XPS) technique equipped with an Al $K\alpha$ source (excitation energy = 1486.7 eV). The film surface was sputtered using Ar gas for 10 min to record the XPS spectra of Ni film. The spectrum for carbon was taken for reference and a survey scan was taken in coarse steps (0.5 eV) to obtain the constituents of the film. After that, fine scans with a step size of 0.02 eV were taken near the edge region. Energy shifts, if any, were corrected with respect to the carbon 1s spectrum.

The soft X-ray reflectivity (SXR) of the sample was measured using the soft X-ray reflectivity beamline (BL-03) (Modi *et al.*, 2019) at the Indus-2 synchrotron source. The SXR data were recorded in the photon energy range 500–1500 eV. The beamline is equipped with a varied-line-spacing plane grating monochromator (VLS-PGM) which operates in constant deviation angle geometry. The beamline provides photons in the energy range 100–1500 eV with moderate resolution of 1000–6000 using three gratings with line densities of 150, 400 and 1200 lines mm^{-1}. The beamline operating in an ultra-high-vacuum environment is separated from experimental station working in $\sim 10^{-7}$ mbar using a custom-designed differential pumping system. The reflectivity measurements are performed in s-polarization geometry with the goniometer working in the vertical dispersion geometry. The sample stage and the goniometer are electrically isolated from each other, which facilitates the measurement of total electron yield current of the sample directly by connecting a wire to the sample surface. The reflected beam from the

sample is measured using a Si photodiode detector (International Radiation Detectors Inc., USA) with 100% internal quantum efficiency.

2.3. Data analysis

Reflection spectroscopy is a powerful technique to determine structural and optical properties of materials. When a material is illuminated by electromagnetic radiation, X-ray specular reflection occurs as a response of the material according to Snell's law. Measurements of the reflectivity data contain information about both the real and imaginary parts of the refractive index.

During X-ray reflectivity measurements, phase information is lost as only reflected intensity is recorded. Phase information of the complex reflection coefficient is necessary to determine δ and β from the reflectivity data. To find the phase information, Kramers–Kronig relations can be applied on the reflectivity data using the relation (Nash et al., 1995)

$$\phi(\omega) = -\frac{2\omega}{\pi} \, \mathrm{PV} \int_0^{+\infty} \frac{\ln R(\omega', \theta)}{\omega'^2 - \omega^2} \, d\omega'. \tag{1}$$

Here, PV refers to the principal value of the integral, ω is the angular frequency of the incident X-ray wavefield and $R(\omega', \theta)$ is the reflectivity measured at grazing-incidence angle θ as a function of ω'. Once the phase information is extracted from the measured reflectivity data, the complex reflection coefficient can be obtained,

$$r(\omega) = \sqrt{R(\omega)} \, \exp\left[i\phi(\omega)\right]. \tag{2}$$

Equation (2) can be equated with the Fresnel's equation of s-polarized light for grazing-incidence angle θ to determine complex refractive index n,

$$r(\omega) = \frac{\sin\theta - (n^2 - \cos^2\theta)^{1/2}}{\sin\theta + (n^2 - \cos^2\theta)^{1/2}}. \tag{3}$$

Complex refractive index n is defined as $n = 1 - \delta + i\beta$. The Kramers–Kronig analysis of the reflectivity data thus provides information about δ and β.

## 3. Results and discussions

3.1. GIXRR and XPS results

Fig. 1 shows the measured and fitted GIXRR spectra of the Ni thin film. The data were fitted using different models with two-, three- and four-layer structures. The best fit was obtained using a three-layer model consisting of a native oxide layer on the substrate, a principal nickel layer and a top surface layer formed due to oxidation or contamination. The formation of a ~20 Å thin oxide layer on top of a Ni film is also reported by Diel et al. (1997). A schematic of the three-layer model used for GIXRR analysis is shown in the inset of Fig. 1. From the GIXRR fit the thickness of the principal nickel layer is found to be 112 Å with r.m.s. roughness of 4 Å. The top surface layer and native oxide layer on the substrate are found to be 22 Å and 34 Å thick with r.m.s. roughness of
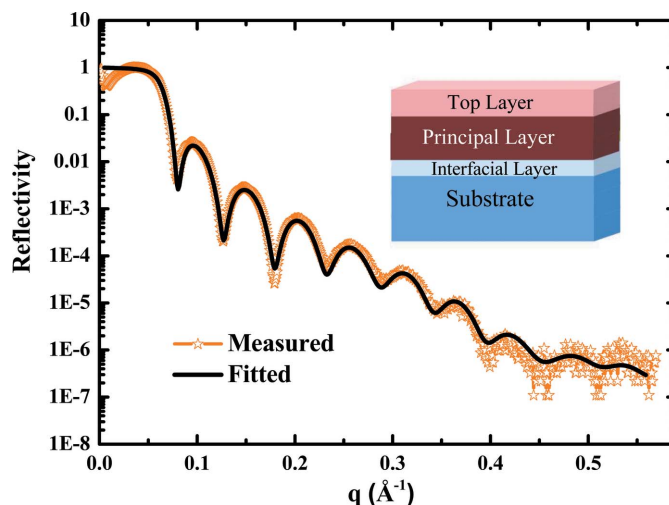
Figure 1
Measured and fitted GIXRR spectra of the Ni thin film. A schematic of the model used to obtain the best fit is also shown.

2 Å and 5 Å, respectively. The fitting of the GIXRR data gives structural parameters as well as complex scattering length density (SLD). The real and imaginary parts of this quantity are related to electron density and the absorption of the material, respectively. The scattering length density profile hence obtained is shown in Fig. 2. From the analysis, the density of the principal nickel layer is found to be 9.26 g cm^{-3} which is slightly higher (~4%) than its bulk density (8.9 g cm^{-3}).

In the survey scan of the XPS measurements, different sharp peaks corresponding to main constituents nickel, carbon and oxygen are observed. High-resolution core spectra of the Ni 2p level and O 1s level are shown in Fig. 3. The data were analysed using XPSPEAK 4.1 software. Background subtraction was performed using a Shirley background. Different sub-peaks along with a linear combination of Lorentzian and Gaussian peak profiles were included to fit the data with minimum chi-squared values. The elemental composition of the film was obtained from the calculation of the peak area (I) and relative sensitivity factor (RSF) using
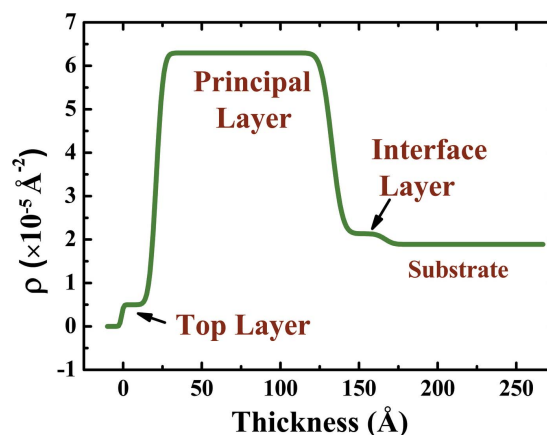
Figure 2
Scattering length density profile of the Ni film as obtained from the analysis of GIXRR data.
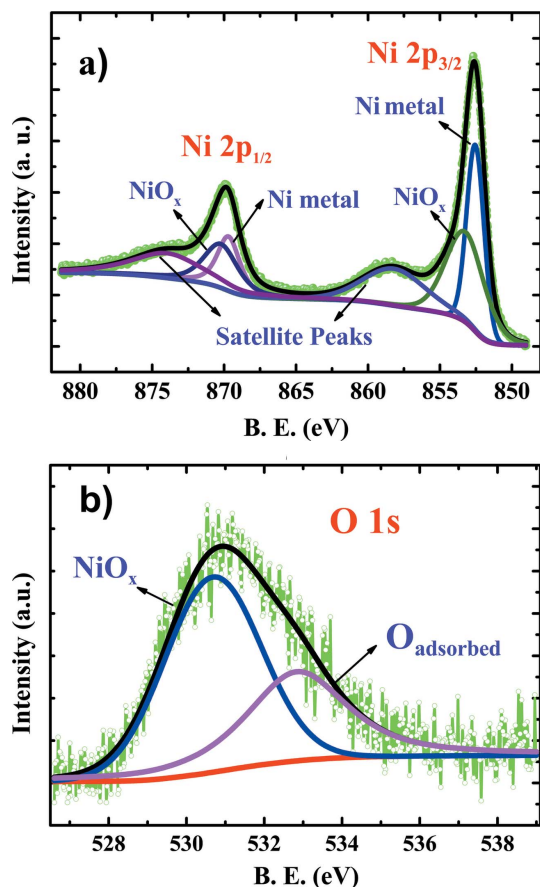
Figure 3
XPS spectra of the (a) Ni 2p core level and (b) O 1s core level.

$$\frac{n_a}{n_b} = \frac{I_a (\text{RSF})_b}{I_b (\text{RSF})_a}. \tag{4}$$

Here, n_a and n_b are atomic concentrations of elements a and b, respectively, in the sample.

For the case of the Ni $2p_{3/2}$ core level [Fig. 3(a)], the spectrum was fitted using two peaks centred at 852.9 eV and 853.6 eV along with a satellite peak at 858.2 eV (Hüfner, 1995). The spin orbital splitting of the $2p$ states of Ni was also taken into account to fit the complete spectrum. The peak at 852.9 eV can be attributed to pure Ni and that at 853.6 eV to some oxide of Ni (NiO$_x$) present due to surface oxidation (Grosvenor *et al.*, 2006; Al-Kuhaili *et al.*, 2015). From these two peak parameters it was found that, in the top few ångströms of the film, 46% of nickel is present as metallic Ni, whereas the rest of it is bonded with oxygen. The stoichiometry of the oxide layer on the surface is found from the analysis of the oxygen 1s spectrum [Fig. 3(b)]. For the O 1s core level, the spectrum was fitted using two peaks at 531.0 eV and 533.2 eV. The peak at 531.0 eV corresponds to the oxygen bonded with Ni to form NiO$_x$ and that at 533.2 eV to the adsorbed oxygen present in the surface layer (Liu *et al.*, 2016). From the area under the peaks and RSF for Ni $2p_{3/2}$ (14.6) and oxygen (0.57), the ratio of nickel to oxygen is found to be 0.7 in NiO$_x$. So, the surface layer comprises Ni with an oxidation state between +2 and +3.

3.2. Soft X-ray optical response

To obtain the soft X-ray optical response of the nickel thin film, reflectivity versus angle measurements at different incident photon energy were carried out. The measured SXR data were analysed using the Parratt formalism keeping the structural parameters (thickness and roughness) fixed as obtained from the analysis of the GIXRR spectrum. This leaves δ and β of each layer as the only variable parameters and, thus, reduces the number of variables for the chi-squared optimization process thereby improving the accuracy of the refined parameters. The best fitted spectra are shown in Fig. 4. Analysis of the SXR spectra gives δ and β for all three layers of the model used for fitting the data. The optical constants of the principal nickel layer are considered for discussion in the following text.

Angle-dependent reflectivity data provide information on the optical constants at discrete photon energies. In order to obtain the optical constants in the continuous energy range, energy-dependent reflectivity measurements are performed in the energy region spanning the Ni $L_{2,3}$ absorption edge at
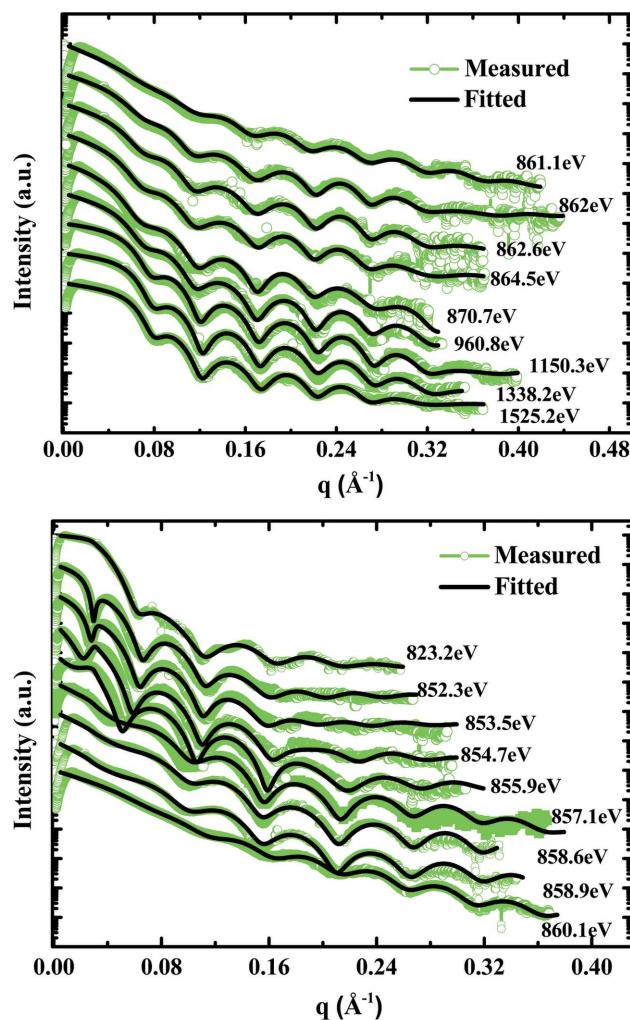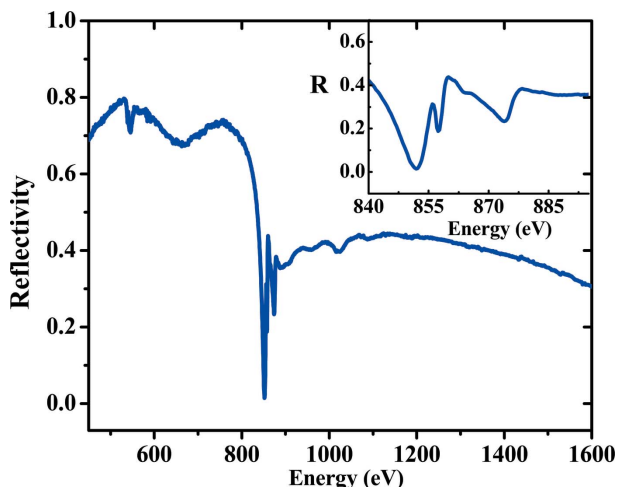

Figure 4
Measured and fitted angle-dependent SXR spectra of the Ni thin film for different incident photon energies as indicated in the graph.
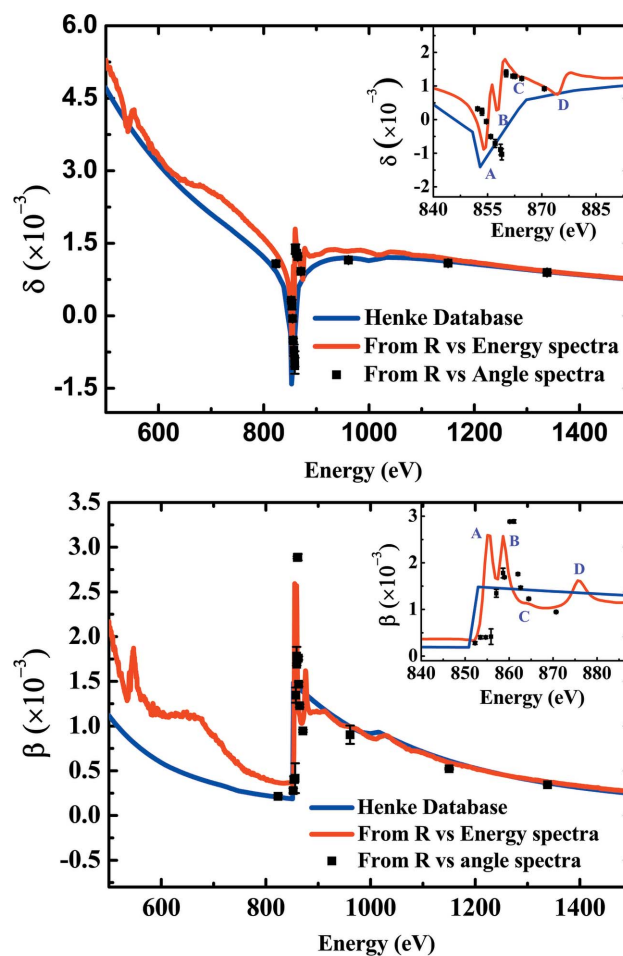
Figure 5
Measured energy-dependent reflectivity spectrum of the Ni thin film at fixed 2° grazing-incidence angle.

fixed grazing-incidence angles of 2° and 3°. Fig. 5 shows the R versus photon energy spectra obtained at 2° grazing-incidence angle. To obtain the complex reflection coefficient, the phase information is determined using the Kramers–Kronig relations [equation (1)]. From the information of the complex reflection coefficient, Fresnel's equations [equation (3)] for s-polarized light were inverted to obtain the optical constants for the whole energy range. It is to be noted that the depth probed by the incident photons during energy-dependent reflectivity measurements varies with energy (Henke *et al.*, 1993; Attwood, 1999). In the vicinity of the Ni L-edge, the penetration depth of incident photons lies in the range of 40–70 Å in the energy region 820–840 eV, which then increases to more than 200 Å at the absorption edge energy. As we go to energies above the absorption edge (854 eV and beyond), the penetration depth of the photons varies between 20 and 40 Å. This suggests different depth regions in the sample are probed at different incident energies.

In Fig. 6, optical constants obtained from the angle-dependent SXR data as well as from the energy-dependent SXR data are plotted along with Henke's tabulated data (Henke *et al.*, 1993). Optical constants values obtained from the angle-dependent SXR data correspond to the principal Ni layer as the optical constants of the oxidized surface layer are represented by a separate layer. Experimentally obtained optical constants are consistent with Henke's tabulated values for photon energies above the L absorption edge of nickel. However, below the absorption edge region, the signature of oxygen is present at ∼542 eV which is in agreement with GIXRR and XPS measurements, and significant deviations from the tabulated values are observed which is likely to be due to high absorption by oxygen. Near the edge region, β values of the tabulated data show a step-function-like behaviour, with no signature of spin orbit splitting of the L-edge. Contrary to the tabulated data, distinct features corresponding to spin orbit splitting of the L-edge are clearly visible in the experimentally determined optical constants. In addi-

tion to $L_{2,3}$ splitting, a few other features are also observed. The optical constants profile obtained from angle-dependent and energy-dependent reflectivity measurements follow the same behaviour, with slight deviations near absorption edge regions. This can be attributed to the uncertainties in the parameters obtained from fitting of data. The accuracy of optical constants obtained from the angle-dependent data depends on the β/δ ratio of the material (Soufli & Gullikson, 1997). It has been shown that, for $\beta/\delta < 1$, the reflectivity shows a step-function-like behaviour near the critical angle and the critical angle is uniquely defined by $\theta = \sqrt{2\delta}$. Hence, the values of δ and β can be determined uniquely. As the ratio increases to unity and beyond, the reflectivity shows an exponential behaviour (André *et al.*, 1984). The step-function-like behaviour disappears and it becomes difficult to locate the critical angle position. Therefore, the uncertainty in the determination of the optical constants increases. In our case, the ratio β/δ becomes greater than unity near the absorption edge region, thus increasing the uncertainties in the obtained optical constants from angle-dependent reflectivity data.

Figure 6
Measured optical constants of the Ni thin film obtained from the reflectivity versus photon energy data are shown along with the corresponding curves obtained from the tabulated data (Henke *et al.*, 1993).

The optical constants obtained from energy-dependent reflectivity measurements show several fine features, marked in Fig. 6 as A ($\sim$854 eV), B ($\sim$858 eV), C ($\sim$864 eV) and D ($\sim$874 eV), which provide insight into the electronic structure of nickel. The ground state of atomic nickel is $[Ar]3d^8 4s^2$, which mainly consists of the ^3F state in accordance with Hund's rule. However, due to configuration interaction between the $3d$ and $4s$ states, the ground state of Ni comprises superposition of $3d^8 4s^2$, $3d^9 4s^1$ and $3d^{10} 4s^0$ valence states with relative weights 15–20%, 60–70% and 15–20%, respectively (Jo & Sawatzky, 1991; Magnuson et al., 1998). Near absorption edge energies, transitions of electrons from $2p^6 3d^9$ to $2p^5 3d^{10}$ states take place. Hence the features B ($\sim$854 eV) and D ($\sim$874 eV) correspond to these transitions from $2p_{3/2}$ (L_3) and $2p_{1/2}$ (L_2) core levels to $2p^5 3d^{10}$ final states. However, due to charge transfer effects in valence states of metallic Ni, transitions from ground state to $2p^5 3d^9$ final states have finite probability which leads to satellite peaks (marked as C at $\sim$864 eV) in the absorption spectrum of nickel. Final states $2p^5 3d^9$ resulting from transitions from the $2p^6 3d^8$ ground state also add to the intensity of satellite transitions. These transitions have been attributed to features observed at energies 4 eV above the absorption edge energies in the magnetic circular dichroism spectrum of nickel (Jo & Sawatzky, 1991; Chen et al., 1991). The final states ($2p^5 3d^9$) in these cases are characterized by a hole in the core as well as valence states and are strongly correlated for transition metals (de Groot, 2005). The core hole interaction between core hole and valence hole modifies the effective charge on the Ni atom and simultaneously induces local charge transfer excitations in the valence shells of the atom, which have d character due to configuration interaction between $3d$ shells and sp bands above the Fermi level (Ufuktepe et al., 2011). This results in shake-up satellite features at energies 6 eV above the absorption edge energies. Thus, satellite transitions in nickel correspond to the presence of two-hole final states and are attributed to critical points in the band structure of Ni (Tjeng et al., 1993; Magnuson et al., 1998).

Experimentally determined optical constants of nickel contain several fine features corresponding to spin-orbital splitting (marked as B and D) and satellite transitions (marked as C) which were absent in the tabulated data. However, another feature, marked A, is also observed which could not be related to any known transitions in nickel and seems peculiar. Further studies are being carried out to understand its origin.

4. Conclusions

In the present study, angle-dependent and energy-dependent reflectivity measurements are carried out to obtain the optical constants profile of Ni thin film in the energy region 500–1500 eV. The measured optical constants data show the presence of distinct fine features near the $L_{2,3}$ absorption edge of nickel which are reported for the first time in the measured optical constants profile of nickel. Near the edge region the observed features are explained from the charge transfer effects in the $3d$ shell and core-hole interaction in the $2p$ levels of Ni and correspond to different final states. The optical constants profile obtained from reflectivity data reflects the local structure as well as electronic properties of nickel. Thus, core-hole interactions and charge transfer effects affect the optical properties of Ni and must be considered while evaluating its applications.

References

Al-Kuhaili, M. F., Ahmad, S. H. A., Durrani, S. M. A., Faiz, M. M. & Ul-Hamid, A. (2015). Mater. Sci. Semicond. Process. 39, 84–89.

André, J. M., Barchewitz, R., Maquet, A. & Marmoret, R. (1984). Phys. Rev. B, 29, 6576–6585.

Attwood, D. (1999). Soft X-rays and Extreme Ultraviolet Radiation. Cambridge University Press.

Chen, C. T., Smith, N. V. & Sette, F. (1991). Phys. Rev. B, 43, 6785–6787.

Croce, P. & Névot, L. (1976). Rev. Phys. Appl. (Paris), 11, 113–125.

Cruz, W. de la, Soto, G. & Yubero, F. (2004). Opt. Mater. 25, 39–42.

Delmotte, F., Meyer-Ilse, J., Salmassi, F., Soufli, R., Burcklen, C., Rebellato, J., Jérome, A., Vickridge, I., Briand, E. & Gullikson, E. (2018). J. Appl. Phys. 124, 035107.

Diel, I., Friedrich, J., Kunz, C., Di Fonzo, S., Müller, B. R. & Jark, W. (1997). Appl. Opt. 36, 6376–6382.

Filatova, E., Lukyanov, V., Barchewitz, R., André, J. M., Idir, M. & Stemmler, P. (1999). J. Phys. Condens. Matter, 11, 3355–3370.

Filatova, E., Lukyanov, V., Blessing, C. & Friedrich, J. (1996). J. Electron Spectrosc. Relat. Phenom. 79, 63–66.

Groot, F. (2005). Coord. Chem. Rev. 249, 31–63.

Grosvenor, A. P., Biesinger, M. C., Smart, R. S. C. & McIntyre, N. S. (2006). Surf. Sci. 600, 1771–1779.

Henke, B. L., Gullikson, E. M. & Davis, J. C. (1993). At. Data Nucl. Data Tables, 54, 181–342.

Hüfner, S. (1995). Photoelectron Spectroscopy – Principles and Applications. Berlin/Heidelberg: Springer-Verlag.

Jo, T. & Sawatzky, G. A. (1991). Phys. Rev. B, 43, 8771–8774.

Lagomarsino, S., Jark, W., Di Fonzo, S., Cedola, A., Mueller, B., Engström, P. & Riekel, C. (1996). J. Appl. Phys. 79, 4471–4473.

Liu, A., Liu, G., Zhu, H., Shin, B., Fortunato, E., Martins, R. & Shan, F. (2016). Appl. Phys. Lett. 108, 233506.

Magnuson, M., Wassdahl, N., Nilsson, A., Föhlisch, A., Nordgren, J. & Mårtensson, N. (1998). Phys. Rev. B, 58, 3677–3681.

Modi, M. H., Gupta, R. K., Kane, S. R., Prasad, V., Garg, C. K., Yadav, P., Raghuvanshi, V. K., Singh, A. & Sinha, M. (2019). AIP Conf. Proc. 2054, 060022.

Nash, P. L., Bell, R. J. & Alexander, R. (1995). J. Mod. Opt. 42, 1837–1842.

Parratt, L. G. (1954). Phys. Rev. 95, 359–369.

Peng, J., Li, W., Huang, Q. & Wang, Z. (2016). Sci. Rep. 6, 31522.

Sella, C., Youn, K., Barchewitz, R., Arbaoui, M. & Krishnan, R. (1988). Appl. Surf. Sci. 33–34, 1208–1215.

Singh, A., Sinha, M. & Modi, M. H. (2018). Vacuum, 155, 60–63.

Sinha, M., Modi, M. H., Ghosh, H., Yadav, P. K. & Gupta, R. K. (2018). *J. Synchrotron Rad.* **25**, 771–776.

Soufli, R. & Gullikson, E. M. (1997). *Appl. Opt.* **36**, 5499–5507.

Spiga, D., Pareschi, G., Citterio, O., Banham, R., Basso, S., Cassanelli, M., Cotroneo, V., Negri, B., Grisoni, G., Valsecchi, G. & Vernani, D. (2004). *Proc. SPIE*, **5488**, 813–819.

Takenaka, H., Kawamura, T. & Kinoshita, H. (1996). *Thin Solid Films*, **288**, 99–102.

Tjeng, L. H., Chen, C. T., Rudolf, P., Meigs, G., van der Laan, G. & Thole, B. T. (1993). *Phys. Rev. B*, **48**, 378–382.

Ufuktepe, Y., Akgül, G., Aksoy, F. & Nordlund, D. (2011). *X-ray Spectrom.* **40**, 427–431.

Waki, I., Hirai, Y., Momose, A. & Hayakawa, K. (1989). *Rev. Sci. Instrum.* **60**, 2072–2075.

Xu, H., Yang, L. H., Da, B., Tóth, J., Tőkési, K. & Ding, Z. J. (2017). *Nucl. Instrum. Methods Phys. Res. B*, **406**, 475–481.